



Article

Study on g-C₃N₄/BiVO₄ Binary Composite Photocatalytic Materials

Pengfei Li ^{1,†}, Yanqiu Hu ^{1,†}, Di Lu ¹, Jiang Wu ^{2,*} and Yuguang Lv ^{1,*}¹ College of Pharmacy, Jiamusi University, Jiamusi 154007, China² School of Stomatology, Jiamusi University, Jiamusi 154007, China

* Correspondence: wujiangwj0126@163.com (J.W.); yuguanglv@163.com (Y.L.); Tel.: +86-139-4546-6344 (J.W.); +86-186-9709-7060 (Y.L.)

† These authors contributed equally to this work.

Abstract: Recent studies have shown that the composite of semiconductor photocatalytic materials and g-C₃N₄ can effectively inhibit photocatalytic carrier recombination and enhance the adsorption performance of the composite photocatalytic materials, so that the composite photocatalyst has stronger photocatalytic activity. In this paper, three kinds of graphitic carbon nitride photocatalyst g-C₃N₄ with different morphologies were prepared using the same precursor system by the chemical cracking method. After characterization and application, the sample with the most significant photocatalytic activity was selected and the g-C₃N₄/BiVO₄ heterostructure was synthesized by the simple solvent evaporation method, then the photocatalytic experiment was carried out. The results show that, when the content of BiVO₄ in the composite sample is 1%, the photocatalytic activity of RhB was the highest, and the degradation rate could reach 90.4%. The kinetic results showed that the degradation of RhB was consistent with the quasi-primary degradation kinetic model. The results of the photocatalytic cycle experiment show that the photocatalytic performance remains unchanged and stable after four photocatalytic cycles. The existence of a g-C₃N₄/BiVO₄ binary heterojunction was confirmed by UV/Visible diffuse reflection (UV-DRS) and photoluminescence (PL) experiments. Owing to the Z-type charge process between BiVO₄ and g-C₃N₄, efficient carrier separation was achieved, thus enhancing the photocatalytic capacity. This work provides a new idea for the study of heterojunction photocatalytic materials based on g-C₃N₄.



Citation: Li, P.; Hu, Y.; Lu, D.; Wu, J.; Lv, Y. Study on g-C₃N₄/BiVO₄ Binary Composite Photocatalytic Materials.

Micromachines **2023**, *14*, 639. <https://doi.org/10.3390/mi14030639>

Academic Editors: Qingyou Lu and Qiyuan Feng

Received: 24 February 2023

Revised: 1 March 2023

Accepted: 8 March 2023

Published: 11 March 2023



Copyright: © 2023 by the authors. Licensee MDPI, Basel, Switzerland. This article is an open access article distributed under the terms and conditions of the Creative Commons Attribution (CC BY) license (<https://creativecommons.org/licenses/by/4.0/>).

Keywords: BiVO₄; g-C₃N₄; photocatalytic

1. Introduction

Semiconductor photocatalysts have become increasingly well known in recent decades. They have been paid attention because of their advantages, such as being green, no pollution, high efficiency, energy saving, stability, and low price. Photocatalysis technology has shown excellent performance in improving the environment, making it one of the research hotspots in pollutant degradation [1–4]. Currently, the most used catalysts are TiO₂ [5–7] and ZnO [8–11], among others. However, their catalytic performance is not efficient. In visible light, the utilization rate of light is low, which limits its application in real life scenarios. Therefore, a new type of photocatalyst needs to be prepared to compensate for the shortcomings of conventional catalysts.

g-C₃N₄ [12–14] has the advantages of narrow band gap, low cost, acid and alkali resistance, and environmental protection. Therefore, g-C₃N₄ has become a hot research topic in recent years, although monomeric g-C₃N₄ has some defects, such as low utilization of sunlight and fast photogenerated carrier complexation. These defects hinder its application in the process of environmental treatment. In order to improve the defects existing in g-C₃N₄, as well as to improve the photocatalytic activity of g-C₃N₄, modification research has been carried out. Different methods such as doping [15–17], morphology control [18,19], and surface loading [20] can be used.

BiVO_4 [21–23] is a potential functional semiconductor material discovered in recent years. Thanks to its advantages such as a wide source of constituent elements; excellent physical, chemical, and thermal stability; being non-toxic and harmless; and narrow band gap, BiVO_4 can be excited to generate photogenerated electrons and holes under visible light, so as to realize more effective utilization of solar energy. It has recently become one of the hot spots in the field of photocatalysis. However, the electrons in BiVO_4 move at a slow rate, resulting in about 60–80% of the resulting charge carriers recombining before they reach the surface. The photogenerated electron hole pairs in BiVO_4 materials are difficult to separate and easy to recombine. At present, no single BiVO_4 material can achieve its theoretical photoelectric conversion efficiency. However, owing to the particularity of the band structure, the heterojunction composite semiconductor photocatalyst can greatly improve the separation efficiency of electron–hole pairs and produce responses to most spectral frequencies, so as to improve the photocatalytic efficiency.

To sum up, three kinds of $g\text{-C}_3\text{N}_4$ with different morphologies were prepared using urea as the precursor system. The best morphology was $g\text{-C}_3\text{N}_4$ by B characterization and performance analysis, the Z-type heterojunction GCB composite samples were successfully prepared by combining with BiVO_4 , and its catalytic activity was determined by the photocatalytic degradation of rhodamine B (RhB) under visible light irradiation. The photocatalytic reaction mechanism is also presented. This study provides a reference for the further development and reference of $g\text{-C}_3\text{N}_4$.

2. Materials and Methods

2.1. The Preparation of $g\text{-C}_3\text{N}_4$

Here, 10 g of melamine was placed into an alumina crucible to form a semi-closed space. The crucible was placed in a muffle furnace under the protection of an air atmosphere; after heating to 500 °C for 2.5 h, deamination polymerization was carried out. After cooling to room temperature, yellow bulk $g\text{-C}_3\text{N}_4$ samples were obtained, named $g\text{-C}_3\text{N}_4\text{-b}$.

2.2. The Preparation of Sheet $g\text{-C}_3\text{N}_4$

The $g\text{-C}_3\text{N}_4\text{-b}$ was ground into powder, 10 mL of 2 mol/L H_3PO_4 was added, and it was stirred at room temperature for 30 min, followed by ultrasonic stirring for 30 min. The mixture was transferred to a reaction kettle, heated at 160 °C in a constant temperature blast drying oven for 4 h, then cooled to room temperature, cleaned three times with deionized water and anhydrous ethanol, and dried for 8 h to obtain the sheet $g\text{-C}_3\text{N}_4$ sample—named $g\text{-C}_3\text{N}_4\text{-s}$.

2.3. The Preparation of $g\text{-C}_3\text{N}_4$ Tube

The $g\text{-C}_3\text{N}_4\text{-s}$ was ground into powder and 10 mL of 2 mol/L $\text{NH}_3\cdot\text{H}_2\text{O}$ was added. It was dispersed uniformly by ultrasound for 30 min, then transferred to a reaction kettle, stored at 180 °C in a constant temperature blast oven for 4 h, cooled to room temperature, and washed three times with deionized water and anhydrous ethanol to obtain the tubular $g\text{-C}_3\text{N}_4$ sample—named $g\text{-C}_3\text{N}_4\text{-t}$.

2.4. Three Kinds of $g\text{-C}_3\text{N}_4$ Morphologies Were Evaluated in Photocatalytic Experiments

The photocatalytic degradation of photocatalysts was evaluated using rhodamine B as an organic dye model. Here, 0.5 g $g\text{-C}_3\text{N}_4\text{-b}$, $g\text{-C}_3\text{N}_4\text{-s}$, and $g\text{-C}_3\text{N}_4\text{-t}$ were weighed into three beakers and 100 mL of 20 mg/L RhB solution was added to each beaker; RhB solution was used as the source of pollution and the samples were magnetically stirred in the dark for 30 min. After adsorption equilibrium, a xenon lamp of 350 watts was irradiated as the visible light source. The absorbance of 5 mL samples was measured every 30 min. The maximum absorption wavelength was 553 nm and it was measured with an ultraviolet visible spectrophotometer.

$$\text{Degradation rate of RhB} = \frac{C_t}{C_0} \times 100\% \quad (1)$$

where C_t is the concentration of RhB measured after a period of reaction and C_0 is the concentration at the beginning of the reaction. The degradation rate of Rhodamine for the three samples was calculated, and the sample with the highest degradation rate was selected for reserve.

2.5. The Preparation of BiVO_4

Here, 0.25 g $\text{Bi}(\text{NO}_3)_3 \cdot 5\text{H}_2\text{O}$ was dissolved in 10 mL of 2 mol/L H_3PO_4 solution and 0.12 g of NH_4VO_3 was dissolved in 10 mL of 2 mol/L $\text{NH}_3 \cdot \text{H}_2\text{O}$ solution. The two were slowly mixed so that they were stirred evenly, and the pH of the mixed solution was adjusted to 7. After the above process, a uniform clear yellow suspension was formed. The solution was transferred to the reactor and kept in a constant temperature blast oven at 160 °C for 8 h. It was then cooled to room temperature, subjected to high-speed centrifugation, washed several times with deionized water and anhydrous ethanol, and dried at 60 °C for 8 h, thus BiVO_4 was obtained.

2.6. The Preparation of Z-Type Heterojunction $g\text{-C}_3\text{N}_4/\text{BiVO}_4$

The $g\text{-C}_3\text{N}_4$ sample with the best 5 g degradation effect was dissolved in 10 mL of ethanol solution, and the $g\text{-C}_3\text{N}_4$ was evenly dispersed by ultrasonic treatment. BiVO_4 with mass fractions of 0.3%, 0.5%, 1%, 3%, and 5% was added. After continuous agitation, the pH of the solution was adjusted to 7. Cooling to room temperature, high-speed centrifugal treatment, centrifugation with deionized water and anhydrous ethanol, washing for several times, and drying at 60 °C for 8 h were carried out to obtain Z-type heterojunction $g\text{-C}_3\text{N}_4/\text{BiVO}_4$, named GCB-x ($x = 0.3\%$, 0.5%, 1%, 3%, and 5%, respectively). When testing its photocatalytic performance, the experimental steps are the same as in Section 2.4.

2.7. Characterization Method

The information of substance composition and crystal structure can be obtained by XRD characterization; the model of XRD equipment used in this study is XDR-6100 and the scanning range is 10°–80°. The infrared spectrometer is IS10 with a scanning range of 500–4000 cm^{-1} . SEM uses secondary electronic signal imaging to observe the surface morphology and structure of the sample. This article is used for research. XPS can determine the composition and state of atoms or ions in the surface layer of an unknown sample. The XPS used in this study are AXIS ULTRA devices from Shimadzu, Japan. The instrument used was a Nicolet 5700 infrared spectrometer to test the molecular structure inside the material. In the test process, KBr and the tested sample were mixed and ground at a ratio of 100:1, and then pressed to test the transmittance. Photoluminescence (PL) is the process by which a substance absorbs a photon and radiates it back. PL spectrum can characterize the defects, impurities, and luminescence properties of semiconductor materials. Fluoro Max-4p is the PL spectrometer used in this study, with a Xenon lamp with an excitation source of 150 W and excitation wavelength of 425 nm. A UV-4100 UV/Visible spectrophotometer (Hitachi, Tokyo, Japan) was used to obtain the visible diffuse spectra (UV/Vis diffuse reflectance spectra, DRS) to test the absorbance change in the powder sample with wavelength change; the scanning range is 200 nm–800 nm.

2.8. Evaluation of the Photocatalytic Mechanism

The light absorption characteristics of the samples were studied by solid UV/Vis DRS. This method was used to analyze the displacement of the side band and the change in the forbidden band gap between them. The band gap of the sample can be calculated using the formula below.

$$\alpha h\nu = A (h\nu - E_g)^{n/2} \quad (2)$$

where α is the absorption coefficient, $h\nu$ is the photon energy, A is a constant equal to 1, and E_g is the band gap energy. The values of n are 4 for indirect transition and 1 for direct

transition [24]. The valence and conduction band potentials of $g\text{-C}_3\text{N}_4$ and BiVO_4 can be calculated using their electronegativity with the following empirical equations.

$$E_{\text{VB}} = X + 0.5E_{\text{g}} - E_{\text{e}} \quad (3)$$

$$E_{\text{CB}} = E_{\text{VB}} - E_{\text{g}} \quad (4)$$

Here, E_{CB} and E_{VB} represent the conduction band edge and valence band edge, respectively; X is the absolute electronegativity of the semiconductor; and E_{e} is a measurement scale factor of the redox level of the reference electrode relative to the absolute vacuum scale [25].

3. Results

Figure 1a shows massive $g\text{-C}_3\text{N}_4\text{-b}$, with many layers and serious agglomeration and a small specific surface area, which is not conducive to the photocatalytic reaction. Figure 1b shows $g\text{-C}_3\text{N}_4\text{-s}$, which has thin lamella and a relatively uniform distribution. Figure 1c shows $g\text{-C}_3\text{N}_4\text{-t}$. It can be seen that the rough surface and large specific surface area provide more active sites, which is conducive to the construction of the semiconductor heterojunction and improving the catalytic activity of the catalyst [26].

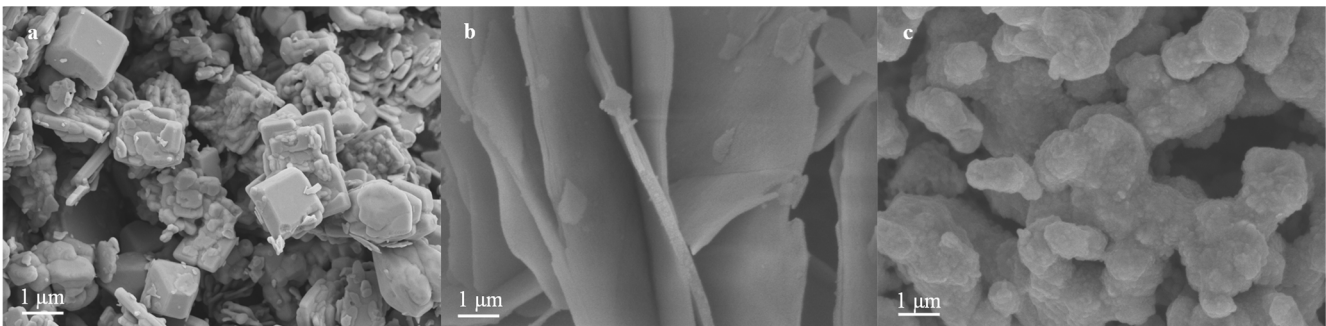


Figure 1. SEM diagram of (a) $g\text{-C}_3\text{N}_4\text{-b}$; (b) $g\text{-C}_3\text{N}_4\text{-s}$; and (c) $g\text{-C}_3\text{N}_4\text{-t}$.

The XRD pattern of the $g\text{-C}_3\text{N}_4$ photocatalyst is shown in Figure 2a. It shows that $g\text{-C}_3\text{N}_4\text{-t}$, $g\text{-C}_3\text{N}_4\text{-s}$, and $g\text{-C}_3\text{N}_4\text{-b}$ all have two characteristic peaks. The diffraction peak of $g\text{-C}_3\text{N}_4$ at 27.5° is the typical superposition reflection between layers of the conjugated aromatic hydrocarbon system, and the small peak at about 13.1° corresponds to the (100) diffraction plane of $g\text{-C}_3\text{N}_4$. It can also be seen from Figure 2a that the diffraction intensity of plane (100) and (002) in $g\text{-C}_3\text{N}_4\text{-s}$ is weaker than that of plane $g\text{-C}_3\text{N}_4\text{-b}$ and $g\text{-C}_3\text{N}_4\text{-t}$, which may be because of the fact that the CO_2 produced by C and O in urea during the long calcination of t inhibits the growth of the crystal surface, thus forming structural defects in the sample. Figure 2b shows the FT-IR spectrum of the prepared sample. The spectra of pure $g\text{-C}_3\text{N}_4\text{-t}$, $g\text{-C}_3\text{N}_4\text{-s}$, and $g\text{-C}_3\text{N}_4\text{-b}$ all showed the characteristic peak of $g\text{-C}_3\text{N}_4$. The results showed that multiple peaks in the range of $1230\text{--}1650\text{ cm}^{-1}$ were caused by C=N: 1637 cm^{-1} was attributed to C=N and $1235\text{ cm}^{-1}\text{--}1574\text{ cm}^{-1}$ was attributed to aromatic C-N. The wide peak centered on $3180\text{--}3440\text{ cm}^{-1}$ was attributed to N-H. At 1574 cm^{-1} , the absorption peak strength of $g\text{-C}_3\text{N}_4\text{-t}$ is higher than that of $g\text{-C}_3\text{N}_4\text{-s}$ and $g\text{-C}_3\text{N}_4\text{-b}$, indicating that $g\text{-C}_3\text{N}_4\text{-t}$ has good crystallinity and structural integrity, which is consistent with the XRD results. Figure 2c shows that the three samples have strong fluorescence emission peaks at 547 nm and $g\text{-C}_3\text{N}_4\text{-b}$ has a higher fluorescence intensity, while the $g\text{-C}_3\text{N}_4\text{-t}$ form has a lower fluorescence intensity. The results showed that the position of the emission peak remained unchanged after morphology regulation, but the fluorescence intensity was relatively reduced. Therefore, $g\text{-C}_3\text{N}_4\text{-t}$ fluorescence intensity was the lowest, facilitating the separation of photogenerated carriers and effectively improving the photocatalytic activity.

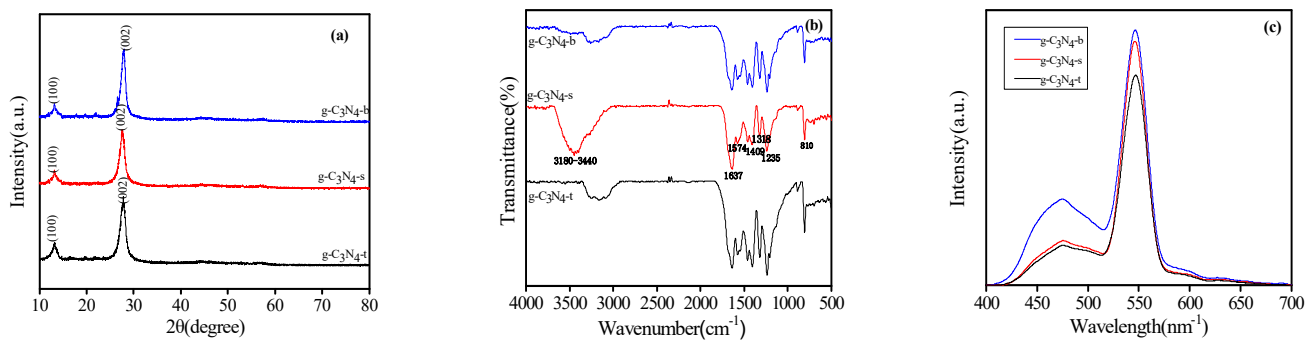


Figure 2. (a): XRD diagram of $g\text{-C}_3\text{N}_4\text{-b}$, $g\text{-C}_3\text{N}_4\text{-s}$, and $g\text{-C}_3\text{N}_4\text{-t}$. (b): FT-IR diagram of $g\text{-C}_3\text{N}_4\text{-b}$, $g\text{-C}_3\text{N}_4\text{-s}$, and $g\text{-C}_3\text{N}_4\text{-t}$. (c): PL diagram of $g\text{-C}_3\text{N}_4\text{-b}$, $g\text{-C}_3\text{N}_4\text{-s}$, and $g\text{-C}_3\text{N}_4\text{-t}$.

Figure 3a shows the degradation effect of pollutants. With the passage of light time, the characteristic absorption peak of RhB in the UV/Visible absorption spectrum weakens synchronously, and no new absorption peak appears in the whole spectrum. When the characteristic absorption peak decreases, it indicates that the concentration of the RhB specific hair group decreases, and the solution gradually becomes transparent, so it can be proved that the pollutant is decomposed at a certain rate. Figure 3b shows the comparison curve of the degradation effect of the synthesized sample on RhB, and it can be seen that the RhB aqueous solution does not easily degrade naturally under visible light radiation, while $g\text{-C}_3\text{N}_4\text{-t}$ showed the best photocatalytic activity. For the data results in Figure 3b, the relationship curve of $-\ln(C_t/C_0)\text{-t}$ is used to represent the first-order reaction kinetics model of the degradation effect in Figure 3c. As shown in Figure 3c, the fitted relationship curve of $-\ln(C_t/C_0)\text{-t}$ is a straight line, and the correlation coefficients R^2 of the line system are all greater than 0.98, which proves that the photodegradation reaction of this series of synthesized samples follows the first-order reaction kinetics law. As the apparent kinetic constant of the quasi-first-order photocatalytic degradation reaction is positively correlated with its photocatalytic activity, under the same experimental conditions, the photocatalytic activity order of the sample is $g\text{-C}_3\text{N}_4\text{-t} > g\text{-C}_3\text{N}_4\text{-s} > g\text{-C}_3\text{N}_4\text{-b}$.

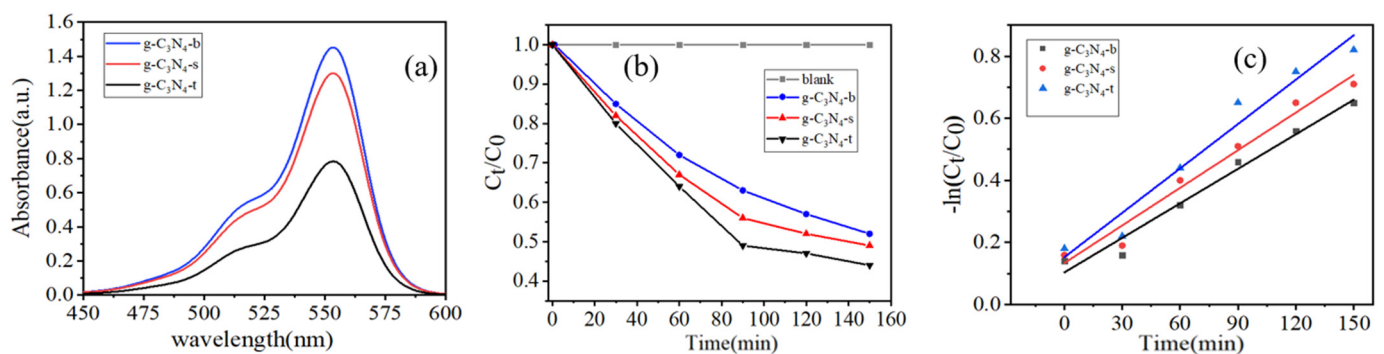


Figure 3. (a): Change in absorbance of Rhodamine B degraded by photocatalyst with time, (b): the comparison curve of the degradation effects of the synthesized sample on RhB, (c): the first-order reaction kinetics curve of the degradation effects of the synthesized sample on RhB.

The morphology, crystal structure, functional group, and fluorescence intensity of three different kinds of $g\text{-C}_3\text{N}_4$ were tested and analyzed in detail. It can be seen from the characterization results that the modified functional groups are not damaged and the crystal structure is not significantly changed, but $g\text{-C}_3\text{N}_4\text{-t}$ has a large specific surface area and can provide more active sites. The fluorescence intensity of $g\text{-C}_3\text{N}_4\text{-t}$ was the lowest, and the photocatalytic activity was improved effectively. The photocatalytic results showed that $g\text{-C}_3\text{N}_4\text{-t}$ had the best degradation effect. Therefore, $g\text{-C}_3\text{N}_4\text{-t}$ was selected for follow-up study.

Figure 4 is a composite sample of $g\text{-C}_3\text{N}_4$ and BiVO_4 . It is hereinafter referred to as GCB. The rough surface of $g\text{-C}_3\text{N}_4$ -t can provide more active sites and promote semiconductor recombination to form a heterojunction, which is conducive to better absorption of visible light and separation of photogenerated charge, thus improving the photocatalytic efficiency.

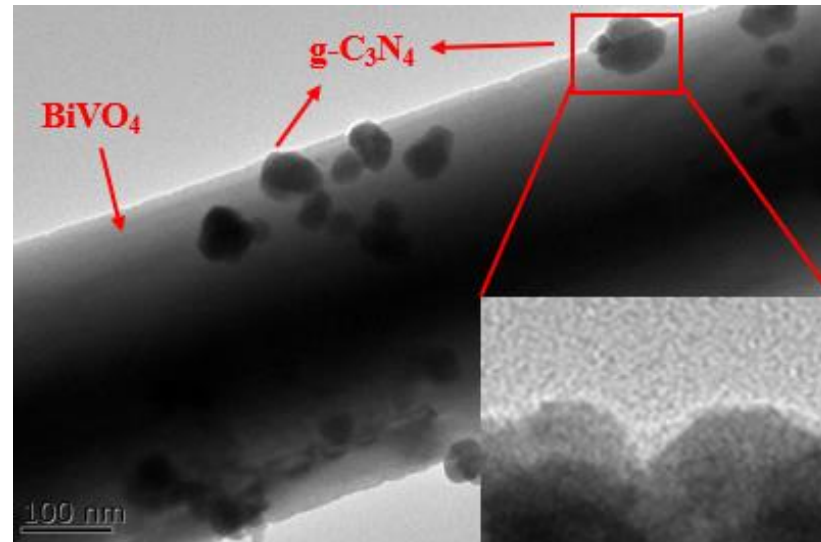


Figure 4. TEM diagram of the composite sample of $g\text{-C}_3\text{N}_4$ and BiVO_4 .

For the $g\text{-C}_3\text{N}_4$ sample, it can be clearly seen that the diffraction peak intensity is the highest at 27.4° , corresponding to the (002) crystal plane, highly consistent with standard cards (JCPDS 87-1526). BiVO_4 has several very obvious characteristic peaks, at 24.52° , 29.08° , 34.49° , and 39.78° . The peak position is basically consistent with the monoclinic crystal of BiVO_4 standard card (JPCDS14-0685). With the increase in BiVO_4 [27] content, the intensity of the diffraction peak gradually increases, indicating that the two are successfully recombined. Figure 5b shows that $g\text{-C}_3\text{N}_4$ at 810 cm^{-1} is attributed to the bending vibration of the hepazine ring system, 1637 cm^{-1} is attributed to $\text{V}_{\text{C}=\text{N}}$, and 1235 cm^{-1} – 1574 cm^{-1} is attributed to aromatic $\text{V}_{\text{C}-\text{N}}$. The wide peak centered on 3180 – 3440 cm^{-1} was attributed to $\text{V}_{\text{N}-\text{H}}$. The corresponding peaks of BiVO_4 at 742 cm^{-1} and 842 cm^{-1} are attributed to $\text{V}_{\sigma_{\text{as}3}}(\text{VO}_4)$ and $\text{V}_{\sigma_{\text{a}1}}(\text{VO}_4)$. The peak intensities of $\text{V}_{\sigma_{\text{as}3}}(\text{VO}_4)$ and $\text{V}_{\sigma_{\text{a}1}}(\text{VO}_4)$ in the GCB composite sample increased slightly with the increase in BiVO_4 content, indicating the existence of two phases in the composite sample. As can be seen from Figure 5c, the emission peaks of BiVO_4 and GCB composite samples appear at 541 nm . The fluorescence intensity of BiVO_4 and $g\text{-C}_3\text{N}_4$ is higher than that of the GCB composite sample, indicating that the photogenerated charges of GCB are more easily separated. It can be seen from the figure that the fluorescence intensity changes with the increase in BiVO_4 content. The sample fluorescence intensity is lowest when the doping amount is GCB-1%. It is speculated that the excess BiVO_4 may cover the active site and reduce the reactive groups.

In order to further characterize the surface chemical composition of $g\text{-C}_3\text{N}_4$, BiVO_4 , and $g\text{-C}_3\text{N}_4/\text{BiVO}_4$ composite catalysts and the interaction between $g\text{-C}_3\text{N}_4$ and BiVO_4 in composite heterojunction materials, we performed XPS tests on pure $g\text{-C}_3\text{N}_4$, BiVO_4 , and GCB-1%. As can be seen from the full spectrum of XPS in Figure 3a, the characteristic absorption peaks on the surface of $g\text{-C}_3\text{N}_4$ are C 1s and N 1s, and those on the surface of BiVO_4 are Bi 4f, V 2p, and O 1s. These absorption peaks are present on the surface of the GCB-1% composite. In $g\text{-C}_3\text{N}_4/\text{BiVO}_4$ composites, the binding energy of C 1s is higher than that of $g\text{-C}_3\text{N}_4$. As shown in Figure 6c, the characteristic peaks of $g\text{-C}_3\text{N}_4/\text{BiVO}_4$ in the composite materials all shifted, indicating that $g\text{-C}_3\text{N}_4$ interacts strongly with BiVO_4 during the formation of the composite catalyst, which increases the binding energy of C 1s and N 1s. As shown in Figure 6d, Bi 4f has two characteristic peaks, and the binding

energies of Bi 4F_{7/2} and Bi 4F_{5/2} are 159.2 eV and 164.5 eV, respectively. As shown in Figure 6e, V 2p has two characteristic peaks, and the binding energies of V 2P_{1/2} and V 2P_{3/2} correspond to 516.8 eV and 523.7 eV, respectively. As shown in Figure 6f, O 1s has three characteristic peaks. Moreover, 529.5 eV represents the lattice O in BiVO₄, and 530.2 eV and 532.3 eV correspond to hydroxyl oxygen and O adsorbed in water on the catalyst surface, respectively. Through the analysis of element species, it was further proved that the GCB composite sample was successfully prepared.

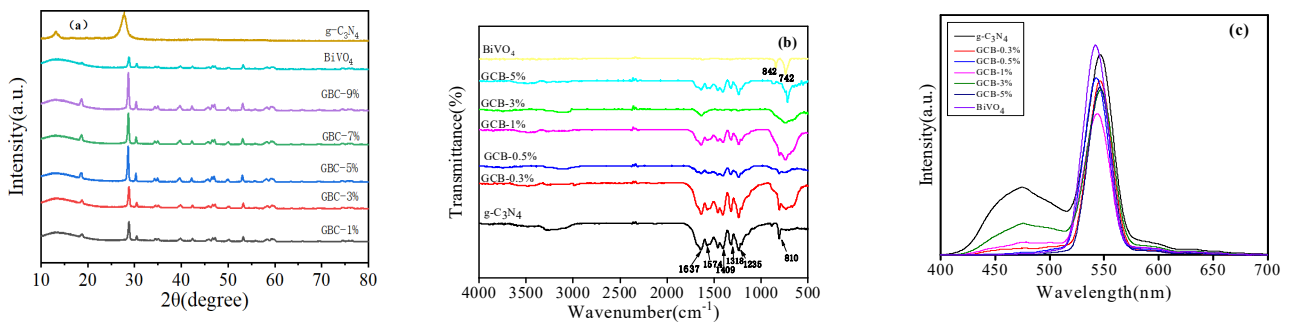


Figure 5. XRD diagram of (a) g-C₃N₄, BiVO₄, GCB composite sample. FT-IR diagram of (b) g-C₃N₄, BiVO₄, GCB composite sample. PL diagram of (c) g-C₃N₄, BiVO₄, GCB composite sample.

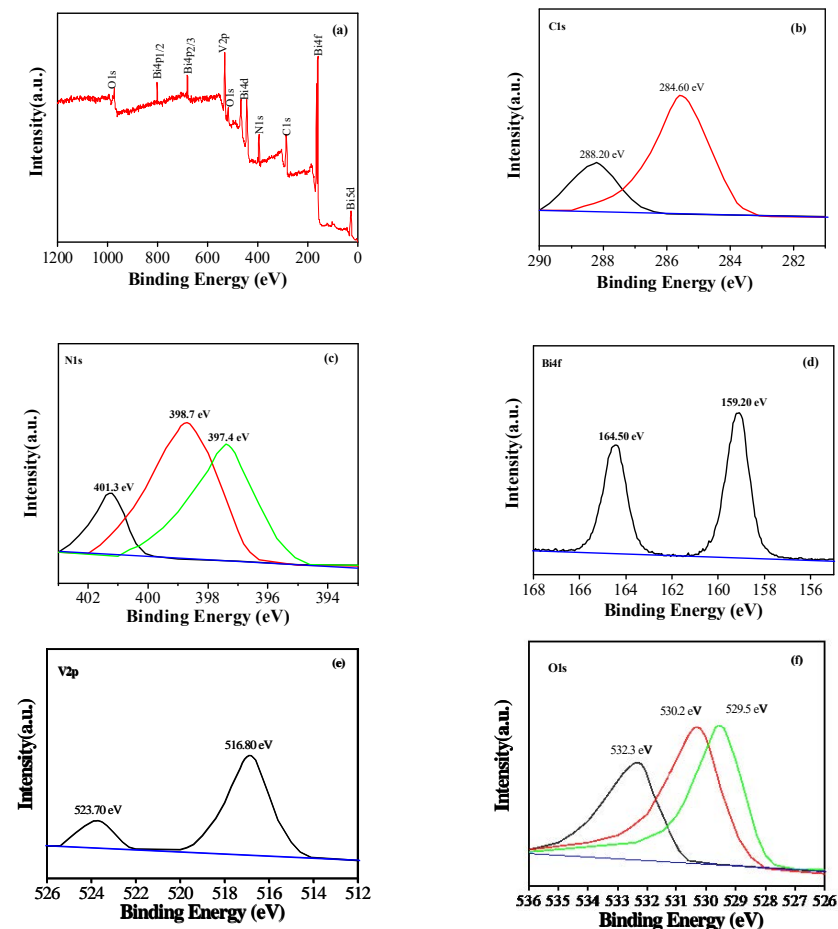


Figure 6. XPS patterns of BiVO₄/g-C₃N₄ samples: full spectrum (a), C 1s (b), N 1s (c), Bi 4f (d), V 2p (e), and O 1s (f).

Figure 7a shows that the GCB composite samples display a red shift phenomenon, and the light absorption capacity is obviously improved. With the increase in BiVO₄ content, the

red shift was more obvious. E_g corresponding to $g\text{-C}_3\text{N}_4$ and GCB composite samples was calculated according to the formula. It can be seen from the figure that the absorption band of $g\text{-C}_3\text{N}_4$ is about 470 nm, $E_g = 2.63$ eV. The absorption band of the GCB composite sample is about 510 nm, $E_g = 2.43$ eV. The results show that the preparation of GCB composite samples reduces the band gap width and improves the visible light response ability of the composite samples.

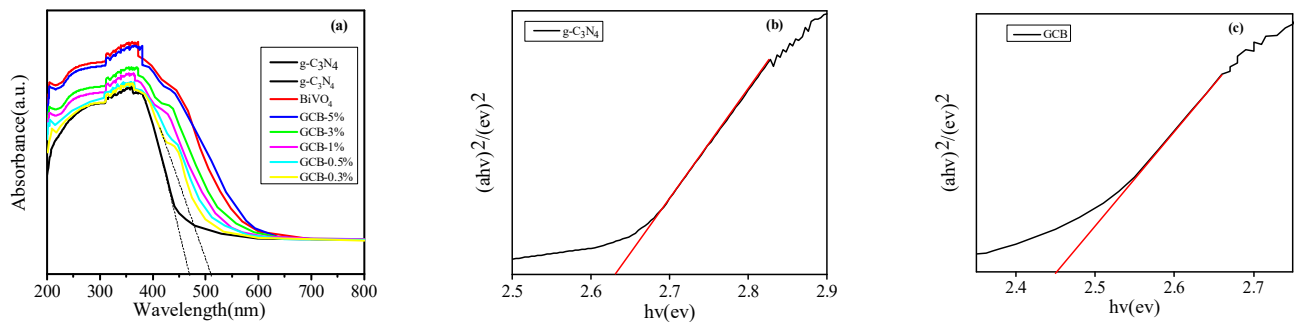


Figure 7. UV/Vis (a) and band gap of (b) $g\text{-C}_3\text{N}_4$ and (c) GCB composite sample.

GCB (m) is a simple physical mixture of $g\text{-C}_3\text{N}_4$ and BiVO_4 , and GCB is a composite catalyst with a heterojunction prepared by the hydrothermal method, Figure 8a shows that, after 30 min reaction in the dark, GCB has a strong adsorption capacity. This is because, in the process of doping, ultrasound can evenly disperse $g\text{-C}_3\text{N}_4$ -t in deionized water, so that GCB has a large specific surface area. The degradation efficiency of GCB (m) was significantly lower than that of GCB during the photoreaction, which was caused by the formation of the Z-type heterojunction between the GCB composite samples. Figure 8b shows that the photocatalytic activity of $g\text{-C}_3\text{N}_4$ -t is low with the increase in time after the dark reaction for 30 min and then light reaction for 300 min. $D_{\text{RhB}} = 33.4\%$. Even though $g\text{-C}_3\text{N}_4$ -t can absorb visible light, the photoelectron-hole pair recombination rate is high, which inhibits their photocatalytic activity. When different BiVO_4 contents were added, the D_{RhB} of the GCB-0.3% sample was 59.6%, that of the GCB-0.5% sample was 63.3%, and that of the GCB-1% sample was 90.4%. However, when the content of BiVO_4 was increased further, the degradation rate did not increase, but rather decreased. It may be that excessive doping of BiVO_4 may attach to the surface of $g\text{-C}_3\text{N}_4$, thus reducing the active site and specific surface area of the surface, resulting in lower degradation efficiency of RhB. Therefore, the degradation rate of RhB reaches 90.4% when the doping amount is GCB-1% under illumination for 300 min, and it has the best catalytic activity.

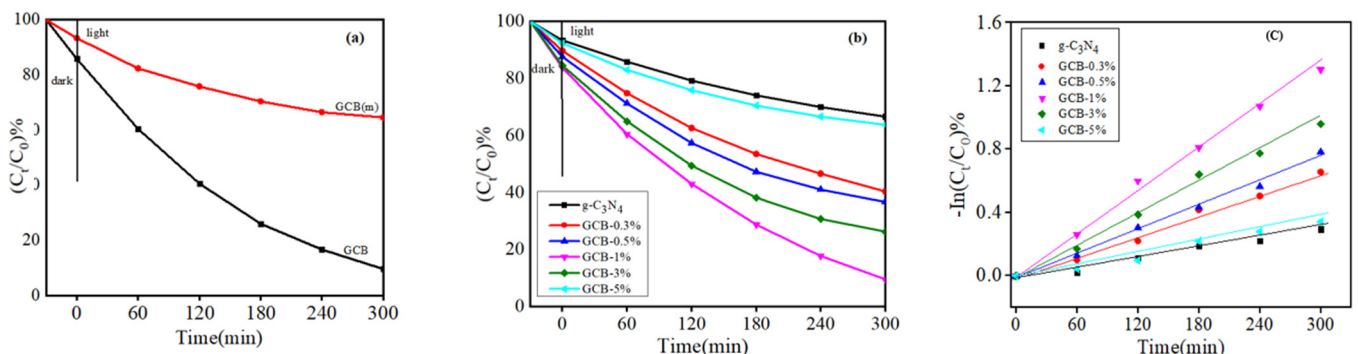


Figure 8. (a) Photocatalytic degradation curves of GCB (m) and GCB; (b) photocatalytic degradation curves of different doping amounts of BiVO_4 ; (c) first-order reaction constants of GCB photocatalytic degradation of RhB.

Table 1 shows that GCB-1% has the highest k value, $k = 0.00434 \text{ min}^{-1}$, indicating that the sample has the best degradation effect on RhB. The correlation coefficients R^2 of

the GCB composite samples are all greater than 0.9, and the results show that the samples conform to the first-order reaction kinetic equation.

Table 1. Linear fitting data of photocatalytic reaction kinetics of GCB composite samples.

The Sample Name	The Regression Equation	k	R ²
g-C ₃ N ₄	Y = 0.0010 - 0.014 x	0.00099	0.9784
GCB-0.3%	Y = 0.0022 - 0.0179 x	0.00219	0.9915
GCB-0.5%	Y = 0.0025 - 0.0134 x	0.00251	0.9932
GCB-1%	Y = 0.0044 + 0.0207 x	0.00434	0.9959
GCB-3%	Y = 0.0033 - 0.0019 x	0.00328	0.9941
GCB-5%	Y = 0.0012 - 0.0174 x	0.00117	0.9808

Figure 9a shows that, after four cycles, the D_{RhB} of the GCB-1% sample decreased somewhat, but the D_{RhB} still remained above 80%, proving that the structure of the prepared GCB sample was not damaged and still had good activity, indicating that the GCB composite sample has good repeatability. As shown in Figure 9b, $D_{RhB} = 90.4\%$ of the GCB-1% sample, while the photocatalytic activity did not change significantly when IPA was added. After EDTA and VC were added, the photocatalytic activity was reduced, with $D_{RhB} = 32.6\%$ and $D_{RhB} = 51\%$. Therefore, the experiment shows that h^+ and $\cdot O_2^-$ are the main active species in the catalytic system of GCB, among which $\cdot O_2^-$ is more important to the degradation of RhB.

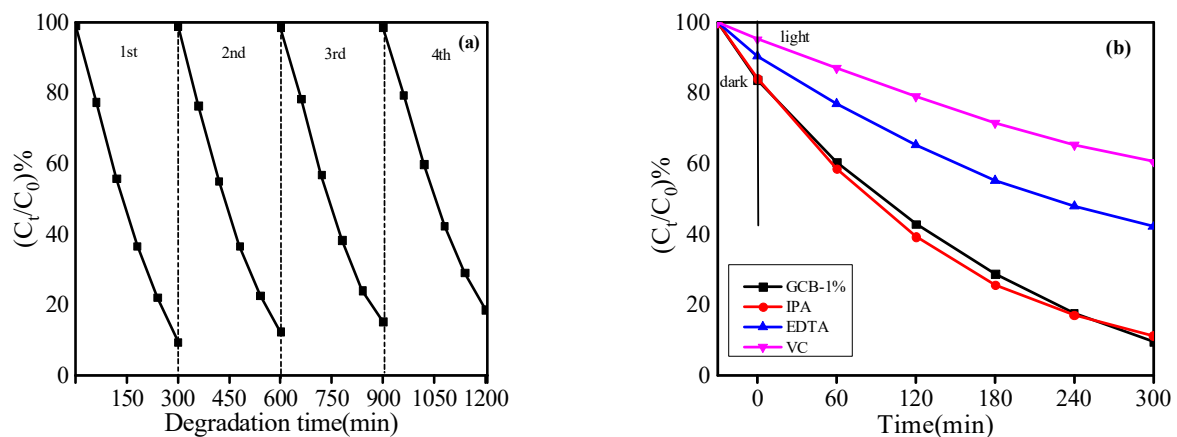


Figure 9. (a) Stability of GCB-1% photocatalytic degradation of RhB dye; (b) the results of the reactive-group-capture experiment for the photocatalytic degradation of RhB by the GCB-1% sample.

Figure 10 is a diagram of the photocatalytic reaction mechanism. The crystal structure of $BiVO_4$ is composed of octahedral layers arranged alternately, which is conducive to enhancing the separation of $e^- - h^+$. Table 2 shows that the gap between $CB_{g-C_3N_4}$ and CB_{BiVO_4} (1.62 eV) is much larger than that between VB_{BiVO_4} and $VB_{g-C_3N_4}$ (1.37 eV), so the e^- of CB_{BiVO_4} is easily transferred to $VB_{g-C_3N_4}$. As a result, the e^- of CB_{BiVO_4} and h^+ of $VB_{g-C_3N_4}$ are easily recombined, and more e^- reduced oxygen molecules on $CB_{g-C_3N_4}$ produce $\cdot O_2^-$. Therefore, the photocatalytic activity of GCB samples was significantly enhanced. It can be concluded that $g-C_3N_4 / BiVO_4$ is a Z-type heterojunction photocatalyst.

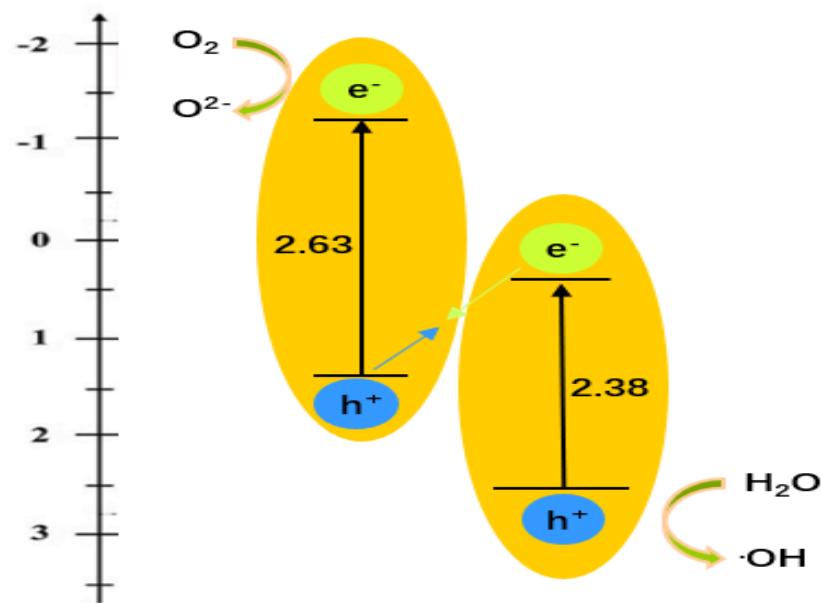


Figure 10. Diagram of the photocatalytic mechanism.

Table 2. Band gap energy (eV) and conduction band and valence band potential (V) of g-C₃N₄ and BiVO₄.

Semiconductors	E _g (eV)	CB (eV)	VB (eV)
g-C ₃ N ₄	2.63	−1.15	1.48
BiVO ₄	2.38	0.47	2.85

4. Conclusions

Three kinds of g-C₃N₄ with different morphologies were prepared using urea as the precursor system. The best morphology was g-C₃N₄-t, by B characterization and performance analysis, and the Z-type heterojunction GCB composite samples were successfully prepared by combining with BiVO₄, and were characterized by various methods. In order to test the photocatalytic activity of GCB-1%, the degradation experiment of RhB aqueous solution was carried out. The stability and photocatalytic mechanism of Z-type heterojunction GCB-1% composite samples were discussed. TEM shows that doping BiVO₄ increases the contact area, improves the separation efficiency of photogenerated charge, and increases the photocatalytic degradation efficiency. XRD shows that the prepared BiVO₄ is monoclinic crystal phase and the prepared g-C₃N₄ is tetragonal phase, indicating that the two are successfully compounded. FT-IR shows that the peak intensities of V_{σas3} (VO₄) and V_{σa1} (VO₄) increase slightly with the increase in BiVO₄ content, indicating the existence of g-C₃N₄ and BiVO₄ phases in the composite sample. PL shows that, when the doping amount is GCB-1%, the fluorescence intensity is the lowest and the photocatalytic ability is the strongest. PL shows that, with the doping amount of GCB-1%, the fluorescence intensity is the lowest, that is, the electron–hole recombination rate is the highest. XPS indicated that the diffraction peaks of C 1s and N 1s in GCB-1% moved in the direction of higher binding energy, and the diffraction peaks of O 1s and Bi 4f moved in the direction of lower binding energy. These changes indicated that g-C₃N₄ interacted with BiVO₄ during the formation of g-C₃N₄/BiVO₄ composites. According to the UV/Vis results, the visible light absorption intensity of GCB composite samples increased, while the gap between the GCB composite samples decreased, indicating that the doped composite samples were more favorable to the improvement in photocatalytic activity. When the doping amount is GCB-1%, D_{RhB} = 90.4% is the highest. The cyclic stability test shows that the GCB-1% composite sample has good repeatability. The results of free radical capture experiments

showed that h^+ and $\cdot O^{2-}$ were the main active components in the GCB catalytic system, and $\cdot O^{2-}$ played a decisive role in the degradation of RhB.

Author Contributions: Methodology, D.L.; Formal analysis, Y.H.; Data curation, J.W.; Writing—original draft, P.L.; Writing—review & editing, Y.L. All authors have read and agreed to the published version of the manuscript.

Funding: This work was financially supported by the Department of Scientific Research project in Heilongjiang province (No. LH2022B022), Jiamusi University horizontal research project (No. 20210428001; No. 2021040301). The young talent innovation project of the education department of Heilongjiang province of China (Grants No.UNPYSCT-2018114).

Data Availability Statement: Subsequent articles need to be used and will not be made public for the time being.

Conflicts of Interest: The funders had no role in the design of the study; in the collection, analyses, or interpretation of data; in the writing of the manuscript; or in the decision to publish the results.

References

1. Oh, V.B.-Y.; Ng, S.-F.; Ong, W.-J. Is photocatalytic hydrogen production sustainable?—Assessing the potential environmental enhancement of photocatalytic technology against steam methane reforming and electrocatalysis. *J. Clean. Prod.* **2022**, *379*, 134673. [[CrossRef](#)]
2. Ismael, M. Environmental remediation and sustainable energy generation via photocatalytic technology using rare earth metals modified g-C₃N₄: A review. *J. Alloys Compd.* **2023**, *931*, 167469. [[CrossRef](#)]
3. Zhao, J.; Sun, J.; Meng, X.; Li, Z. Recent Advances in Vehicle Exhaust Treatment with Photocatalytic Technology. *Catalysts* **2022**, *12*, 1051. [[CrossRef](#)]
4. Jarusheh, H.S.; Yusuf, A.; Banat, F.; Haija, M.A.; Palmisano, G. Integrated photocatalytic technologies in water treatment using ferrites nanoparticles. *J. Environ. Chem. Eng.* **2022**, *10*, 108204. [[CrossRef](#)]
5. Liu, X.; Duan, X.; Bao, T.; Hao, D.; Chen, Z.; Wei, W.; Wang, D.; Wang, S.; Ni, B.-J. High-performance photocatalytic decomposition of PFOA by BiOX/TiO₂ heterojunctions: Self-induced inner electric fields and band alignment. *J. Hazard. Mater.* **2022**, *430*, 128195. [[CrossRef](#)] [[PubMed](#)]
6. Qi, F.; Yang, Z.; Qiu, Q.; Wang, Y.; Li, H. Defective TiO₂ with increased photocatalytic activity synthesized by the TiO₂/Ti interfacial reaction method. *Surf. Interfaces* **2022**, *30*, 101828. [[CrossRef](#)]
7. Fu, J.; Zhang, X.; Li, H.; Chen, B.; Ye, S.; Zhang, N.; Yu, Z.; Zheng, J.; Chen, B. Enhancing electronic metal support interaction (EMSI) over Pt/TiO₂ for efficient catalytic wet air oxidation of phenol in wastewater. *J. Hazard. Mater.* **2022**, *426*, 128088. [[CrossRef](#)]
8. Guo, J.; Han, Y.; Xu, Z.; Zha, W.; Fang, J.; Luo, Q.; Liu, L.; Ma, C.-Q. Monodispersed ZnO nanoink and ultra-smooth large-area ZnO films for high performance and stable organic solar cells. *Flex. Print. Electron.* **2022**, *7*, 025013. [[CrossRef](#)]
9. Liu, X.; Wang, G.; Zhi, H.; Dong, J.; Hao, J.; Zhang, X.; Wang, J.; Li, D.; Liu, B. Synthesis of the Porous ZnO Nanosheets and TiO₂/ZnO/FTO Composite Films by a Low-Temperature Hydrothermal Method and Their Applications in Photocatalysis and Electrochromism. *Coatings* **2022**, *12*, 695. [[CrossRef](#)]
10. Rong, X.; Lu, Y.; Yin, J.; Jiang, H.; Han, S.; Zeng, Y.; Xu, W.; Fang, M.; Cao, P.; Zhu, D.; et al. Electroluminescence enhancement of ZnO nanorod array/GaN heterojunction with MgZnO barrier layer. *J. Lumin.* **2022**, *248*, 118946. [[CrossRef](#)]
11. Ren, L.; Tao, Y.; Ma, S.; Liu, Z.; Yang, M.; Wang, S.; Gao, Z.; Xie, H. Controllable preparation and photocatalytic activity of hierarchical flower-like microspheres clustered by ZnO porous nanosheets. *Chem. Phys.* **2022**, *559*, 111552. [[CrossRef](#)]
12. Cao, L.; Zheng, Z.; Liu, Y.; Li, Z.; Li, Y. Special sea urchin-like CdS/g-C₃N₄ photocatalyst with high specific surface area and efficient charge separation. *J. Mater. Sci.* **2022**, *57*, 17609–17621. [[CrossRef](#)]
13. Zhan, X.; Liu, J.; Zhao, Y.; Sun, Y.; Gao, R.; Wang, H.; Shi, H. MOF-derived tunable spin-state MnIII doped g-C₃N₄ photocatalysts with enhanced photocatalytic activity. *Sep. Purif. Technol.* **2022**, *302*, 122146. [[CrossRef](#)]
14. Ma, Y.; Li, J.; Cai, J.; Zhong, L.; Lang, Y.; Ma, Q. Z-scheme g-C₃N₄/ZnS heterojunction photocatalyst: One-pot synthesis, interfacial structure regulation, and improved photocatalysis activity for bisphenol A. *Colloids Surf. A Physicochem. Eng. Asp.* **2022**, *653*, 130027. [[CrossRef](#)]
15. Cheng, H.F.; Huang, B.B.; Dai, Y.; Qin, X.; Zhang, X. One-step synthesis of the nanostructured AgI/BiOI composites with highly enhanced visible-408 light photocatalytic performances. *Langmuir* **2018**, *26*, 6618–6624. [[CrossRef](#)] [[PubMed](#)]
16. Shan, W.; Liu, T. Er³⁺, Yb³⁺ doping induced core-shell structured BiVO₄ and near-infrared photocatalytic properties. *J. Mol. Catal. A Chem.* **2016**, *416*, 1–9. [[CrossRef](#)]
17. Hirakawa, H.; Shiota, S.; Shiraishi, Y.; Sakamoto, H.; Ichikawa, S.; Hirai, T. Au nanoparticles supported on BiVO₄: effective inorganic photocatalysts for H₂O₂ production from water and O₂ under visible light. *ACS Catal.* **2016**, *6*, 4976–4982. [[CrossRef](#)]

18. Zhang, Y.Y.; Guo, Y.P.; Duan, H.N.; Li, H.; Sun, C.; Liu, H. Facile synthesis of V⁴⁺-self-doped, {010}oriented BiVO₄ nanorods with highly efficient visible 414 light-induced photocatalytic activity. *Phys. Chem. Chem. Phys.* **2018**, *16*, 24519–24526. [[CrossRef](#)] [[PubMed](#)]
19. Zhao, Y.; Xie, Y.; Zhu, X.; Yan, S.; Wang, S. Surfactant-free synthesis of hyperbranched monoclinic bismuth vanadate and its applications in photocatalysis, gas sensing, and lithium-ion batteries. *Chem.-A Eur. J.* **2008**, *2019*, 1601–1606. [[CrossRef](#)] [[PubMed](#)]
20. Zhou, F.Q.; Fan, J.C.; Xu, Q.J.; Min, Y.L. BiVO₄ nanowires decorated with CdS nanoparticles as Z-scheme photocatalyst with enhanced H₂ generation. *Appl. Catal. B Environ.* **2017**, *201*, 77–83. [[CrossRef](#)]
21. Wang, D.; Ren, B.; Chen, S.; Liu, S.; Feng, W.; Sun, Y. Novel BiVO₄/TiO₂ composites with Z-scheme heterojunction for photocatalytic degradation. *Mater. Lett.* **2023**, *330*, 133229. [[CrossRef](#)]
22. Liu, X.; Tang, L.; Zhou, G.; Wang, J.; Song, M.; Hang, Y.; Ma, C.; Han, S.; Yan, M.; Lu, Z. In situ formation of BiVO₄/MoS₂ heterojunction: Enhanced photogenerated carrier transfer rate through electron transport channels constructed by graphene oxide. *Mater. Res. Bull.* **2023**, *157*, 112040. [[CrossRef](#)]
23. Minato, A.; Pan, Z.; Katayama, K.; Sohn, W.Y. Enhancement of photoelectrochemical performance of Bismuth vanadate (BiVO₄)-Based photoanode by building phase-junction configurations. *J. Photochem. Photobiol. A Chem.* **2023**, *434*, 114252. [[CrossRef](#)]
24. Mergen, Ö.B.; Arda, E. Determination of Optical Band Gap Energies of CS/MWCNT Bio-nanocomposites by Tauc and ASF Methods. *Synth. Met.* **2020**, *269*, 116539. [[CrossRef](#)]
25. Zhou, Z.; Li, Y.; Lv, K.; Wu, X.; Li, Q.; Luo, J. Fabrication of walnut-like BiVO₄@Bi₂S₃ heterojunction for efficient visible photocatalytic reduction of Cr (VI). *Mater. Sci. Semicond. Process.* **2018**, *75*, 334–341. [[CrossRef](#)]
26. Wu, B.; Gao, Z.; Lv, Y. Preparation of Graphite Phase Bismuth Carbon Nitride Vanadate Composites and Experimental Analysis of Free Radical Capture. *IOP Conf. Ser. Earth Environ. Sci.* **2021**, *898*, 012025.
27. Lv, K.; Wan, D.; Zheng, D.; Qin, Y.; Lv, Y. Enhancement of visible light photocatalytic activity of BiVO₄ by polypyrrole modification. *J. Alloys Compd.* **2021**, *872*, 159597. [[CrossRef](#)]

Disclaimer/Publisher's Note: The statements, opinions and data contained in all publications are solely those of the individual author(s) and contributor(s) and not of MDPI and/or the editor(s). MDPI and/or the editor(s) disclaim responsibility for any injury to people or property resulting from any ideas, methods, instructions or products referred to in the content.